ACS APPLIED MATERIALS & INTERFACES

Research Article

www.acsami.org

Investigation of $Sm_{0.2}Ce_{0.8}O_{1.9}/Na_2CO_3$ Nanocomposite Electrolytes: Preparation, Interfacial Microstructures, and Ionic Conductivities

Shilong Yin, Yanwei Zeng,* Chuanming Li, Xiaowei Chen, and Zhupeng Ye

State Key Laboratory of Materials-Oriented Chemical Engineering, College of Materials Science and Engineering, Nanjing University of Technology, 5 New Model Road, Nanjing 210009, P. R. China

ABSTRACT: With the analytical grade $Ce(NO_3)_3{\cdot}6H_2O$, $Sm(NO_3)_3{\cdot}6H_2O$, and Na_2CO_3 as starting materials, $Sm_{0.2}Ce_{0.8}O_{1.9}$(SDC)/Na_2CO_3 nanocomposite electrolytes were prepared through a rare-earth/sodium carbonate complex precipitation, prefiring, and sintering operations. The phase components and microstructures were studied and characterized by XRD, FESEM, TEM, and TG-DSC. In particular, the interfacial interactions between the phases of SDC crystallites and amorphous Na_2CO_3 were deliberately probed by Raman and infrared spectroscopies. It has been found that the amorphous carbonates in the SDC/Na_2CO_3 composites are tightly bound to the surface of SDC nanocrystals to form an intimate shell-layer via a long-range interface interaction, characterized by ~8 nm in thickness and a red-shift of 15 cm^{-1} for the Raman symmetrical vibration mode of carbonate ions with reference to the crystalline Na_2CO_3, which is practically enabled to frustrate the crystallization of Na_2CO_3 and enhance the transport properties of oxide ions in the SDC/Na_2CO_3 composite electrolytes because of the disordered interface microstructures. Moreover, smaller SDC nanocrystals were found to achieve higher conductivity enhancements for the SDC/Na_2CO_3 composite electrolytes and the {100} facets on the surface of SDC nanocrystals are believed to be more important than the other facets because of their strong electropositivity. This effect makes the SDC/Na_2CO_3 composite sample prefired at 600 °C realize a much higher ionic conductivity than the samples prefired at the other temperatures.

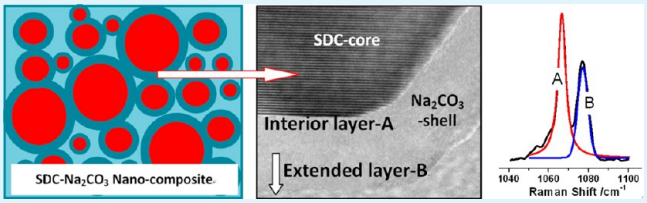

KEYWORDS: *$Sm_{0.2}Ce_{0.8}O_{1.9}$/carbonate composites, SDC nanocrystals, interfacial interactions, microstructures, Raman spectroscopy, ionic conductivity enhancement*

1. INTRODUCTION

Solid oxide fuel cells (SOFCs) are a kind of electrochemical device that can directly convert the chemical energy of hydrogen, methane, methanol, and fossil fuels into electrical energy with the advantages of high overall efficiency, environmental friendliness, and high reliability.[1−4] Nowadays, the high temperature SOFCs based on yttrium-stabilized ZrO_2 (YSZ) electrolytes have shown good performance at high temperatures at ~1000 °C, but the commercialization of SOFCs requires their operation temperatures to be brought down into the intermediate temperature range (IT, 600−800 °C) or even the low temperature range (LT, <600 °C) to expand the utilization of cost-effective materials for bipolar plates and sealing components as well as to avoid the thermal degradation of materials for electrodes and electrolytes, which deteriorates the long-term stability and reliability of SOFCs systems.[5,6] However, this requirement puts forward great challenges to the researchers to develop novel materials for electrodes and electrolytes, which should possess enough high electrochemical activities and ionic conductivities at the intermediate or low temperatures to build up IT-SOFCs or LT-SOFCs with high performance.

Over the past years, a number of new electrolyte materials for intermediate temperature applications have been investigated, such as doped ceria with cubic fluorite type structure and doped lanthanum silicate or germanate with hexagonal apatite type structure, which show higher oxygen ionic conductivities at the intermediate temperatures than the conventional YSZ.[7,8] Among them, moreover, a new category of composite electrolytes composed of ceria-based oxides and alkali carbonates has been found to be of great potentials for applications in IT/LT-SOFCs because of their satisfactorily high overall ionic conductivity, probably arising from the transport of both oxide ions and protons.[9−12] In these two-phase composite materials, the ceria-based oxides include various rare earth doped or co-doped ceria like $Ce_{0.8}Sm_{0.2}O_{1.9}$ (SDC), $Ce_{0.8}Gd_{0.2}O_{1.9}$ (GDC), $Ce_{0.8}Gd_{0.05}Y_{0.15}O_{1.9}$ (GYDC), $Ce_{0.8}Sm_{0.1}Nd_{0.1}O_{1.9}$ (SNDC), and $Ce_{0.8}Sm_{0.2-x}Ca_xO_{2-d}$ (CSDC),[13−17] while the second phase may be one of the Li−Na, Li−K, Na−K binary, and Li−Na−K ternary complex carbonates.

As one of the most extensively studied composite electrolytes of this kind, SDC/carbonate composites often possess much higher ionic conductivities than the single phase SDC (~10^{-3} S cm^{-1} around 600 °C), assuming the conductivity up to ~10^{-1} S cm^{-1} at the intermediate temperatures,[18,19] because of the

Received: August 2, 2013
Accepted: November 19, 2013
Published: November 19, 2013

conductance enhancement by the coexisting alkaline carbonates. Moreover, the single cells based on such composite electrolytes were reported to show excellent performances. J. B. Huang et al.[20] claimed that a peak power density of 950 mW cm^{-2} was achieved at 550 °C on a cell with SDC/25 wt % $LiNaCO_3$ (eutectic composition) as electrolyte. J. Di et al.[21] used similar materials to construct a single cell and reached an output power of 560 mW cm^{-2} at 550 °C. Still, a power density as high as 1700 mW cm^{-2} was accomplished at 650 °C on a cell composed of SDC/$LiNaCO_3$ composite electrolyte.[22] In addition, more recently, the composites of SDC with simple alkali carbonates including SDC/Na_2CO_3 and SDC/K_2CO_3 have been investigated, in which no molten phase is involved at the intermediate temperatures and the conductivity contributions from the mobile ions nonrelated to cathodic and anodic electrochemical reactions are eliminated. Raza et al. reported that use of Na_2CO_3 instead of Li−Na eutectic carbonate may also significantly improve the ionic transport properties with the output power density arriving at 1150 mW cm^{-2} at 500 °C.[23] X. D. Wang et al.[24] prepared the SDC/Na_2CO_3 composite electrolyte with a conductivity of 0.1 S cm^{-1} at around 300 °C and fabricated a single cell with it to reach a power density 800 mW cm^{-2} at 550 °C. N. Zuo et al.[25] attained 602 mW cm^{-2} at 650 °C on a single cell with the SDC/K_2CO_3 electrolyte, whose ionic conductivity was about 0.16 S cm^{-1}. Ma et al. studied the thermal stability of SDC/Na_2CO_3 composites and achieved a steady power density of 620 mW cm^{-2} over 12 h on a single cell with SDC/Na_2CO_3 composite as electrolyte.[26]

To understand how these composite materials can give such excellent properties and then to seek novel electrolyte materials with better performance, over the past years, considerable research efforts have been committed to exploring the enhancement mechanism of ionic conductance in the SDC/carbonate composites. J. B. Huang et al. suggested that there was a space charge region at the interface between SDC particles and carbonate phase,[27] which could enrich oxygen ions at the SDC particle surface and thus induce more oxygen vacancies in SDC bulk in favor of the transport of oxygen ions. Meanwhile, the cations in the interface region of carbonate phase would be enriched because of the electrostatic effect, yielding more cation vacancies inside the carbonate phase to promote the proton conductance, which is often considered to explain the occurrence of water on the cathode side when the SDC/carbonate composite electrolytes are used. Additionally, B. Zhu and X. D. Wang speculated that in SDC/NaK-carbonate composites the oxygen ions would be transported via an oxygen vacancy mechanism inside the SDC particles, while the protons might move along the interface by a "swing" model.[28,29] As regards the SDC/$NaCO_3$ composite electrolytes, B. Zhu et al. proposed that the softening of amorphous Na_2CO_3 in the composite might lead to a remarkable rise in the ionic conductivity around 300 °C and thus contribute to the good performance of the cells.[23,24] Most recently, Q. H. Liu and B. Zhu put forward a theoretical description of superionic conductivity phenomena in SDC/$NaCO_3$ nanocomposites on the basis of effective-medium model.[30] In addition, several interesting research studies on the measurement and comparison of oxide ion conductivity and proton conductivity have been reported,[31−34] in which the different methods were employed for doped-ceria/carbonates composites under the given electrochemical conditions. However, as a matter of fact, the real mechanisms for the ionic conductivity enhancement in SDC/carbonate composites have not yet been clarified and the proposed models or hypotheses mostly remain far from convincing and even controversial because of the scarcity of supportive experimental results and explicit theoretical analyses. Nevertheless, up to now, most researchers interested in this field have recognized that the interactions at the interface between the doped-ceria and the alkali carbonates should make active and crucial contributions to the enhanced ionic conductivities of doped-ceria/carbonate composite electrolytes. Such a fundamental understanding has driven the continuing research in this field. Lately, some wet-chemical approaches, such as the sol−freeze-drying method[35] and one-step co-precipitation method,[36] have been deliberately utilized to prepare the doped-ceria/carbonates composites on nanoscale to create more interfacial area and explore how the adopted chemical processes rouse the interfacial functionalities.

In the present paper, we report on our latest research work concerned with the preparation of SDC/Na_2CO_3 nanocomposite electrolytes and their microstructural investigations by using XRD, FESEM, TEM, and DSC-TG and, especially, putting special emphasis on the probing of the interactions across the interface between the phases of SDC nanocrystals and amorphous Na_2CO_3 by Raman and infrared spectroscopies in an attempt to explore the mechanism responsible for the ionic conductance enhancement in SDC/Na_2CO_3 composite electrolytes. It has been found that there is a long-range interaction between the SDC crystallites and Na_2CO_3 phase, which results in the tight binding of carbonate ions on the facets of SDC nanocrystals and may be well characterized by the shift and broadening of the characteristic Raman spectroscopic peaks of carbonate ions in the samples. From this point of view, the oxide ion transport properties of the composites are discussed in relation to such peculiar interface interactions and the {100} facets of SDC crystallites are believed to play an important role in the conductivity enhancement.

2. EXPERIMENTAL SECTION

According to the chemical formula $Sm_{0.2}Ce_{0.8}O_{1.9}$, stoichiometric amounts of $Ce(NO_3)_3{\cdot}6H_2O$ and $Sm(NO_3)_3{\cdot}6H_2O$ (AR grade) were dissolved together in deionized water to form a 0.5M aqueous solution of nitrate. Then, double amount of 0.5M Na_2CO_3 aqueous solution as a precipitant was poured into the nitrate solution under vigorous stirring to allow a thorough precipitation of carbonate complex $Na[Ce,Sm](CO_3)_2$ by virtue of the reaction $Na[Ce,Sm](CO_3)_2$ (s) = $Na^+ + Ce^{3+}/Sm^{3+} + 2CO_3^{2-}$. The equilibrium constant is as low as log[K] = −17.5 at room temperature[37] and thus expected to produce a precipitate ($Na[Ce,Sm](CO_3)_2$) with a content of 23.49 wt % Na_2CO_3. When the precipitation was completed, the white precipitate was collected through a vacuum filtration and washed three times with deionized water and then dried at 85 °C for 10 h. To investigate the formation of SDC crystallites and structural development of the carbonate phase, the dried precipitate powders were first subjected to a 2 h prefiring at 500, 600, 700, and 800 °C, respectively. After that, the as-fired powders were ground and pressed into pellets with dimensions ⌀12 mm × 0.8 mm at a pressure of 300 MPa and then sintered at 680 °C for 1 h in a muffle furnace.

The phase identification was performed by X-ray diffractometry (XRD, ARL XTRA, Thermo Electron, USA), in which Cu Ka radiation (λ = 1.5406 Å) from a tube powered by 40 kV/35 mA was used to carry out a 2θ scanning from 20° to 80° at a rate of 2° min^{-1} and a goniometric resolution of 0.02°. The morphology and microstructural features of SDC/Na_2CO_3 composite samples were observed by TEM/HRTEM (JEM-2100, JEOL, Japan) and FESEM (Hitachi S-4800, Hitachi, Japan). To trace the possible phase transition in the prefired

precipitate samples, thermal analyses were conducted on a DSC-TG (STA 449C, Netzsch, Germany) in a temperature range from 40 to 500 °C at a heating rate of 5 °C min^{-1} in N_2 flow. The Raman and infrared spectra of the prefired and/or sintered samples were registered on a Raman spectrometer (Lab RamHR800, JYCompany, France) from 200 to 2000 cm^{-1} and a FTIR spectrometer (Nexus 670, Nicolet Co., USA) from 600 to 2400 cm^{-1}. In addition, the sintered disk samples were carefully polished and coated with silver electrodes on the two sides for the measurement of ac impedance spectra, which were carried out from 200 to 600 °C at an interval of 50 °C on an ac impedance spectrometer (Solartron SI-1260) in a frequency range from 0.1 Hz to 1 MHz.

3. RESULTS AND DISCUSSION

3.1. XRD Analysis of Prefired $Na(Ce,Sm)(CO_3)_2$ Precipitates. Figure 1 and Figure 2 show the XRD patterns

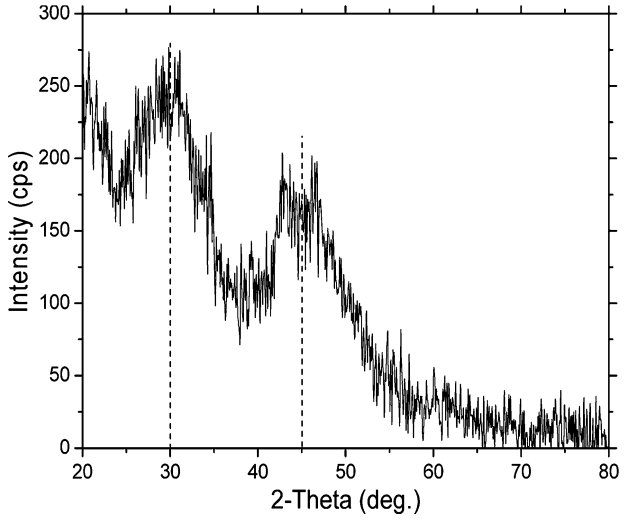

Figure 1. XRD pattern of the dried $Na[Ce,Sm](CO_3)_2$ precipitate powder.

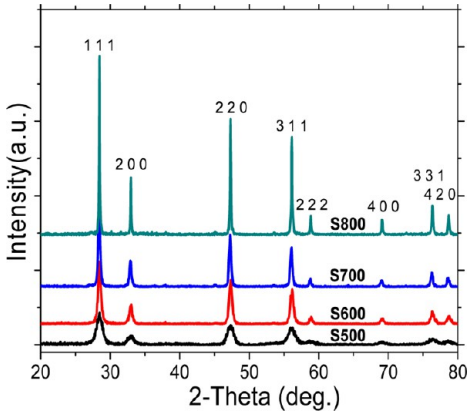

Figure 2. XRD patterns of the $Na[Ce,Sm](CO_3)_2$ precipitate prefired at 500, 600, 700, and 800 °C.

of the dried precipitate and their prefired samples at 500, 600, 700, and 800 °C for 2 h, respectively. It can be seen that the dried precipitate sample exhibits an X-ray diffraction pattern featured with higher intensity at the lower diffraction angle 2θ but modulated by two highly diffuse peaks around 2θ of 30° and 45°. This result seemingly suggests that the dried precipitate is mainly characterized by an amorphous structure, but a certain amount of structurally ordered domains like nuclei prior to crystallization is present within the sample. In contrast, for the prefired precipitate samples, each XRD pattern in Figure 2 shows a set of sharp diffraction peaks attributable to the crystalline SDC (JCPDS card no. 75-0158) and no peaks can be found from the crystalline carbonate or other impurity phases, regardless of their slight differences in the peak profiles. Evidently, it can be determined that the crystalline SDC may be well formed through solid state reactions after the precipitate is prefired for 2 h at 500 °C or higher temperatures, while the carbonate coexisting with SDC is apparently in a noncrystalline state. This suggests that the sodium carbonate phase from the decomposition of $Na[Ce,Sm](CO_3)_2$ is strongly prohibited from crystallization probably because of the interactions across the interface between the freshly borne SDC crystallites and carbonate phase in the prefired SDC/Na_2CO_3 samples.

With the help of Jade 5.0 software, the crystal cell parameters and average grain sizes of the crystalline SDC phases in the different samples were obtained by quantitatively fitting the XRD diagrams, with the best-fit results represented in Figure 3

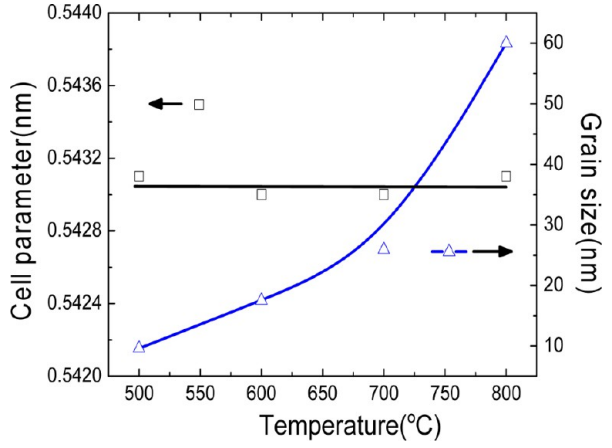

Figure 3. Crystal cell parameters and average grain sizes of SDC crystallites in SDC/Na_2CO_3 composites prefired at 500, 600, 700, and 800 °C.

as a function of prefiring temperature. It can be noted that the cell parameters of SDC phases formed during the different prefiring treatments are of very close values, just varying from 5.430 to 5.431 Å, which are slightly smaller than that given by JCPDS card no. 75-0158, 5.433 Å, but conspicuously larger than the lattice constant of pure CeO_2 (5.411 Å) because of the partial Sm^{3+} substitution for Ce^{4+} in CeO_2. On the other hand, however, the average grain size of SDC crystallites in the prefired samples, which was derived from the Williamson–Hall plot and actually the volume-weighted mean size of coherently crystalline domains, shows a prominent increase from 9.6 nm to 60.0 nm as the prefiring temperature is increased from 500 to 800°C.

3.2. Thermal Analysis of Prefired $Na(Ce,Sm)(CO_3)_2$ Precipitates. To detect any possible phase changes with the prefired SDC/Na_2CO_3 composites in a given temperature range, the prefired samples were analyzed by differential scanning calorimeter and thermogravimeter. Figure 4 shows the typical TG and DSC curves, given by the sample prefired at 800 °C. Obviously, a single endothermic peak at 77 °C along with a weight loss in the TG curve is due to the release of adsorbed water, while no evident endothermic or exothermic effects can be found at temperatures above 120 °C. This result

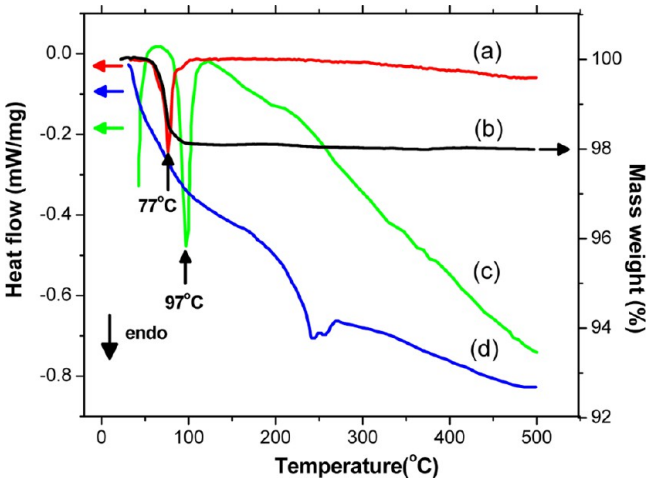

Figure 4. DSC curve (a) and TG curve (b) of SDC/Na_2CO_3 composite obtained after prefiring at 800 °C, with the DSC curves c and d from refs 23 and 24 for comparison.

is quite different from that reported by R. Raza,[23,24] as shown by curves c and d in Figure 4, although the same conditions were used to obtain the SDC/Na_2CO_3 composite samples in this study. R. Raza et al. alleged that besides an endothermic peak at 97 °C for moisture loss, the DSC curve c exhibited a glass transition in the temperature range of 150−200 °C with the SDC/Na_2CO_3 composites and it was believed to enhance the disorderliness of amorphous Na_2CO_3 phase to facilitate the ionic transportation. Taking a close examination of curve c, however, only a subtle rise around 200 °C may be found on the inclined baseline. Moreover, it appears to be exothermic and thus should not be attributed to a glass transition of the amorphous Na_2CO_3. In addition, as shown in Figure 4, curve d is another DSC result for the SDC/Na_2CO_3 composite sample, on which two strong endothermic peaks around 250°C are noted and have also been simply attributed to the glass transition effect.[24] Obviously, they seem to be quite different in thermal effect and should arise from different causes.

3.3. Phases and Microstructures of Sintered SDC/Na_2CO_3 Composites. As shown in Figure 5, the XRD patterns for the SDC/Na_2CO_3 composites sintered at 680 °C for 2 h are apparently the same as those of their prefired samples, regardless of the different details in peak profiles. It means

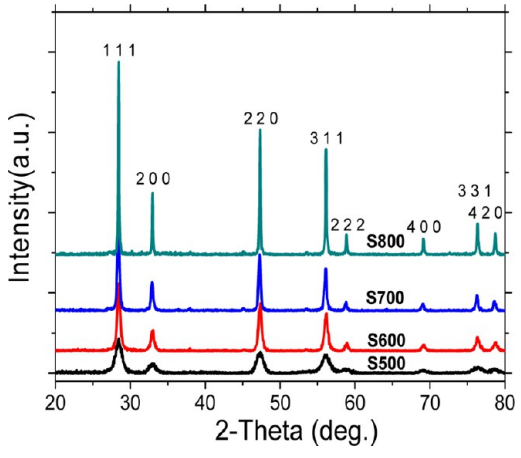

Figure 5. XRD patterns of the SDC/Na_2CO_3 composites sintered at 680 °C after prefiring at 500, 600, 700, and 800 °C.

that the sintered SDC/Na_2CO_3 composites are all made up of the same phase components: crystalline SDC and noncrystalline Na_2CO_3. However, as shown in Figure 6, the quantitative

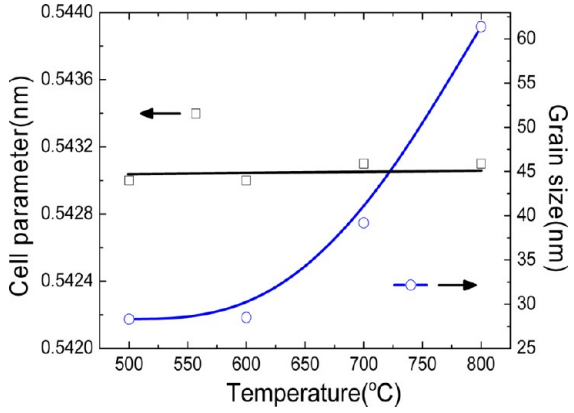

Figure 6. Crystal cell parameters and sizes of SDC crystallites within SDC/Na_2CO_3 composites sintered at 680 °C after prefiring at 500, 600, 700, and 800 °C.

analysis of the XRD data reveals that the SDC crystallites in the sintered samples are quite different in the average grain sizes, which are 28.3, 28.5, 39.2, and 61.4 nm for the sintered samples with prefiring treatments at 500, 600, 700, and 800 °C, respectively, although their cell parameters appear not to change remarkably and remain around 5.430 Å. This result indicates that the SDC crystallites for the samples subject to prefiring at lower temperatures have experienced a more prominent growth in the sintering process than that prefired at higher temperatures and, seemingly, the growth of SDC crystallites is confined to an upper limit by the coexisting amorphous carbonate.

Figure 7 gives two typical SEM images and one HRTEM image for the SDC/Na_2CO_3 composite samples obtained after prefiring at 600 °C and sintering at 680 °C, which demonstrate a structural relationship between the SDC crystallites and amorphous carbonate at a microscopic scale. It can be seen that the SDC crystallites appear to be homogeneously compacted in such a manner that the voids and gaps formed between the individual particles are infiltrated with the amorphous carbonate. Thereby, it can be deduced that the carbonate should form a continuous phase in a three-dimensional network structure in contact with the SDC particles. More interestingly, the high-resolution TEM image in Figure 7c shows the structural details in the interface region between the SDC particles and the neighboring carbonate, in which a distinctive and uniform coating layer of about 8 nm in thickness can be easily identified on the surface of SDC grain, whose lattice fringes give an interplanar spacing of 2.716 Å for the (200) plane. Accordingly, it is reasonable to believe that the carbonate coating layers and the SDC crystallites bounded by them may form the core−shell structured composite particles, and it is the numerous composite particles of this kind that make up the SDC/Na_2CO_3 composite electrolyte. Furthermore, we are convinced that the vast interfacial area between the SDC grains and carbonate shells would yield important contributions to the marvelous properties of SDC/Na_2CO_3 composite materials.

3.4. Raman Spectra of Sintered SDC/Na_2CO_3 Composites. To get an insight into the interface interactions between the SDC nanocrystals and amorphous Na_2CO_3 and their

dx.doi.org/10.1021/am403198x | ACS Appl. Mater. Interfaces 2013, 5, 12876−12886

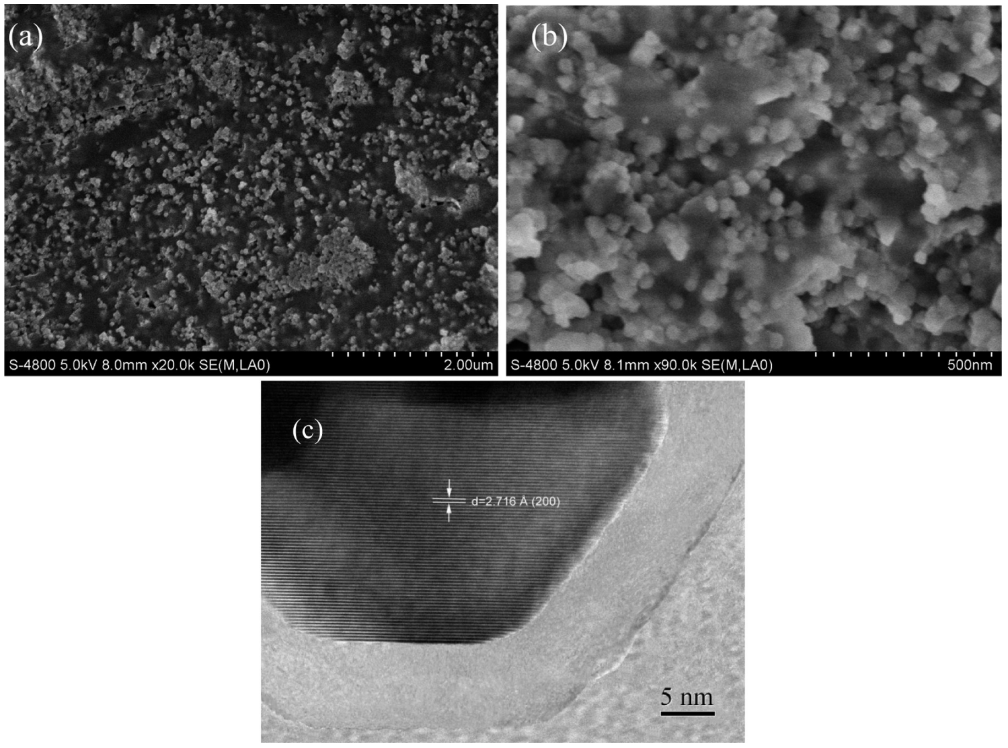

Figure 7. SEM images (a, b) of SDC/Na_2CO_3 composite sintered at 680 °C after prefiring at 600 °C and its HRTEM image (c).

microstructures, Raman spectroscopy was chosen as an effective analytical technique because of its high sensitivity to the local microstructures of materials. As shown in Figure 8, the room temperature Raman spectra of the SDC/Na_2CO_3 composite samples were presented, which are designated with SS500, SS600, SS700, and SS800, respectively, referring to their prefiring temperatures: 500, 600, 700, and 800 °C. The inset gives a magnified view of the Raman spectra from 1050 to 1100 cm^{-1}. For the sake of comparison, the Raman spectra of single phase SDC powder and crystalline Na_2CO_3 are also shown in Figure 8.

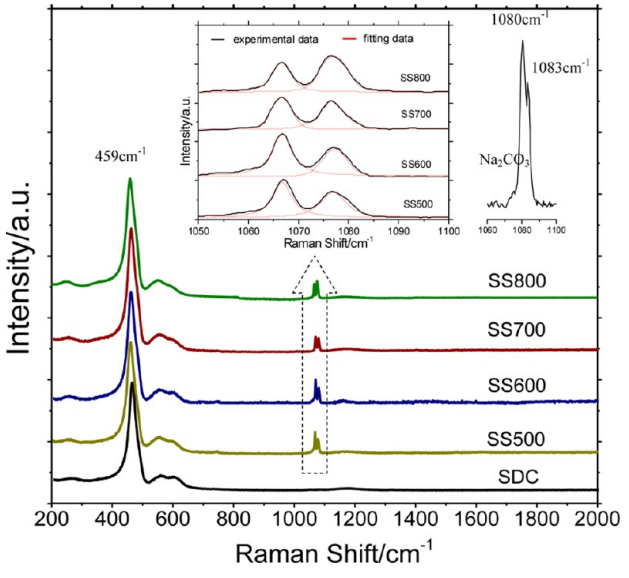

Figure 8. Raman spectra of the SDC/Na_2CO_3 composites sintered at 680 °C after prefiring at 500, 600, 700, and 800 °C, along with that of crystalline Na_2CO_3 and single phase SDC powder.

It can be seen that the SDC/Na_2CO_3 composite samples all exhibit a strong Raman peak at 459 cm^{-1}, which could be attributed to the symmetric breathing mode of Ce/Sm−O_6 octahedrons in the SDC crystal lattice,[38] regardless of a shift to the lower frequency by ∼2 cm^{-1} compared to that of single phase SDC. In addition, two weak and diffuse peaks around 580 cm^{-1} can be noted near this major mode, which are often considered arising from the oxygen vacancies due to the Ce^{4+} substitution by Sm^{3+} ions.[39]

As regards the Raman vibrations from the amorphous carbonate phase in the SDC/Na_2CO_3 composite samples, two relatively weak absorption peaks at ∼1066 and ∼1076 cm^{-1} can be clearly identified, which are quite diffuse and apparently down-shifted by about 15 and 5 cm^{-1}, respectively, in comparison with the Raman spectrum of crystalline Na_2CO_3. It often shows a clear doublet centered at 1081 cm^{-1} with a splitting of ∼3 cm^{-1} at room temperature and was interpreted in terms of an ordered arrangement of CO_3^{2-} ions with two nonequivalent orientations in the primitive cell.[40] Actually, the crystalline γ-Na_2CO_3 is of a typical displace-modulated incommensurate crystal structure in the temperature range from 630 to 130 K. Its strong Raman doublet near 1080 cm^{-1} arises from the symmetrical breathing vibrations of CO_3^{2-} ions with a splitting profile determined by the displace modulation of carbonate ions in the lattice structure.[41,42]

However, in view of the fact that the two Raman peaks for the amorphous Na_2CO_3 phase are quite diffuse and separated by as much as ∼10 cm^{-1}, it should not be reasonable to simply regard them as a doublet corresponding to the one for crystalline Na_2CO_3. Instead, we think that the doublet with small splitting due to the quasi two-state carbonate ions in the crystalline Na_2CO_3 would be no longer observed in the SDC/Na_2CO_3 composites, since a broad range of Raman vibration

states (frequencies) is expected in the amorphous carbonate phase. Thus, the two well-separated and diffuse Raman peaks shown in Figure 8 should exactly reflect a range of different microscopic environments, in which the carbonate ions in the SDC/Na_2CO_3 composites are located. For the sake of simplicity, they may be classified into two distinctive central states, which correspond to the two kinds of physical and chemical microstructures for the carbonate phase in the SDC/Na_2CO_3 composites. Accordingly, considering the formation of carbonate coating layer on the surface of SDC crystallites, it is reasonable to postulate that the Raman peak with the larger down-shift might arise from the carbonate ions in the interior of the shell layers because of their tight binding to the surface of SDC particles, while the peak with the smaller shift should be assigned to those residing off the internal shell layers.

To quantify the differences among the composite samples, the Raman spectra inset in Figure 8 were analyzed by a nonlinear least-squares fitting with the Lorentzian peak function. The resulting peak parameters and curves are presented in Table 1 and Figure 8. It can be noted that, in

Table 1. Raman Peak Parameters for Na_2CO_3 in SDC/Na_2CO_3 Composites

sample	peak position (cm^{-1})	fwhm (cm^{-1})	peak height	relative integrated intensity (%)
SS500	1066.78	4.52	425.54	52.94
	1076.96	6.05	299.43	47.06
SS600	1066.71	4.61	491.51	65.09
	1077.19	5.88	339.05	34.91
SS700	1066.56	3.83	378.65	49.74
	1076.77	4.56	321.58	50.26
SS800	1066.46	3.61	344.00	33.38
	1076.88	5.51	449.87	66.62
Na_2CO_3	1080.21	3.01	319.82	72.51
	1083.44	2.89	189.39	27.49

comparison with the crystalline Na_2CO_3, the Raman peaks for the carbonate in SDC/Na_2CO_3 composite samples all show remarkably large fwhm values, suggesting a broader variety of vibration states for carbonate ions in the amorphous Na_2CO_3 than in the crystalline counterpart, which are believed to have lost long-range order due to the interaction with SDC, as revealed by X-ray diffraction. Besides, the different SDC/Na_2CO_3 samples show the two Raman peaks at close positions around 1067 and 1077 cm^{-1}, respectively, but there are significant differences in their relative integrated intensities. This result indicates that the interactions between the phases of SDC and carbonate may result in two distinctive microscopic environments that are quite similar for different SDC/Na_2CO_3 samples, whereas the relative amounts of carbonate ions belonging to each kind of environment may change significantly from one sample to another on account of their different prefiring conditions. Specifically, the amount of the carbonate ions showing Raman vibrations around 1067 cm^{-1} is first increased from 52.94% (SS500) to 65.69% (SS600) and then decreased to 49.74% (SS700) and 33.38% (SS800) as the prefiring temperature is increased from 500 to 800 °C, featured with the maximum 65.69% for the sample SS600.

As far as the SDC/carbonate interface interactions are concerned, we believed that it is closely associated with the microstructural details of the surface of SDC crystallites. According to the study by D. C. Sayle and W. H. Lee,[43,44] the CeO_2 crystal grains are often bounded with the {100}, {111}, and {110} facets and the surface structural relaxation on these facets may drive Ce^{4+} ions outward to form a positively charged outermost layer,[45] which are coordinated with six oxygen ions in the interior structure. Moreover, in contrast, a higher electropositivity can be established on the {100} facets than on the other facets, as reported by A. Ahniyaz et al.[46] Obviously, the same thing would happen with the Sm-doped CeO_2 crystallites, and the positively charged {100} and {111} facets of SDC nanocrystals in SDC/Na_2CO_3 composites are expected to strongly attract electronegative carbonate groups CO_3^{2-} through a long-range Coulomb force and leave them tightly bound in some manner to reduce the interface energy as much as possible. In this case, under the driving of the principle of energy minimization,[47] part of the oxygen ions relaxed inwards would spontaneously move away to leave more oxygen vacancies $V_o^{\bullet\bullet}$ in the surface zone of SDC crystallites. Obviously, this effect will greatly enhance the transport of oxide ions along the surface layer of SDC crystallites in conjunction with the tightly bound carbonate phase. Moreover, such a transport enhancement of oxide ions should be proportional to the extent to which the carbonate ions are tightly bound on the surface of SDC crystallites.

With the above argument, it can be understood that the carbonate ions bound around the SDC crystallites are actually subjected to an external force from the interfacial interactions, which can be regarded as an equivalent compressive stress on the CO_3^{2-} ions to restrain them from stretching vibrations to some extent. Consequently, the relevant Raman vibrations are expected to show a downward shift depending on the magnitude of the stress. The similar phenomena were observed in the study of Raman spectra of PZT films grown on different substrates, in which the Raman mode shift of PZT films was correlated to their stress states on the basis of the conventional Landau–Devonshire approach and Lyddane–Sachs–Teller relation.[48] Thus, the Raman mode shifts for the amorphous carbonate in SDC/Na_2CO_3 composites provide an evident measure of the interfacial interactions between the phases of SDC and carbonate. In the present case, a red-shift of about 15 cm^{-1} for the Raman peak near 1067 cm^{-1}, arising from the carbonate ions inside the intimate shell layer surrounding the SDC particles, exactly reflects a large Coulomb force imposed on the ions. It is quite large and comparable to the cohering force for the crystalline Na_2CO_3, since the vibration frequency difference between the free CO_3^{2-} ion and the one inside crystalline Na_2CO_3 is just ~20 cm^{-1}.[49] Clearly, the Raman peak down-shifted by ~5 cm^{-1} indicates the presence of a relatively small binding force on the carbonate ions lying off the intimate shell layers. Nonetheless, in view of the magnitudes of the binding forces, they are believed to be strong enough to frustrate the crystallization of Na_2CO_3 in the SDC/Na_2CO_3 composites, as shown by XRD, since the strong long-range Coulomb force would bring about a local deviation in the stoichiometry of Na_2CO_3 and severely evoke a disorder arrangement of sodium and carbonate ions, leading to the amorphous structure. In the same principle, the above understanding can also be applied to explain the appearance of red-shifts in Raman modes for SDC in the SDC/Na_2CO_3 composites. Owing to the strong adsorption of carbonate ions, the compressive stress in the tightly bound layer of carbonate will be inevitably transmitted to the SDC particles surrounded by amorphous Na_2CO_3, and as a result, a red-shift of 2 cm^{-1} is noted in the Raman spectrum of SDC nanocrystals.

In order to further explore the binding states of carbonate ions on the surface of SDC particles, the sintered SDC/Na_2CO_3 samples were soaked for 10 h in deionized water at room temperature to check the dissolution of the carbonate molecules that were bound on the SDC crystallites. After the above treatment, the water-soaked SDC/Na_2CO_3 composites were recovered by centrifuging and drying and found to contain just about 1.5 wt % Na_2CO_3. Figure 9 shows their Raman

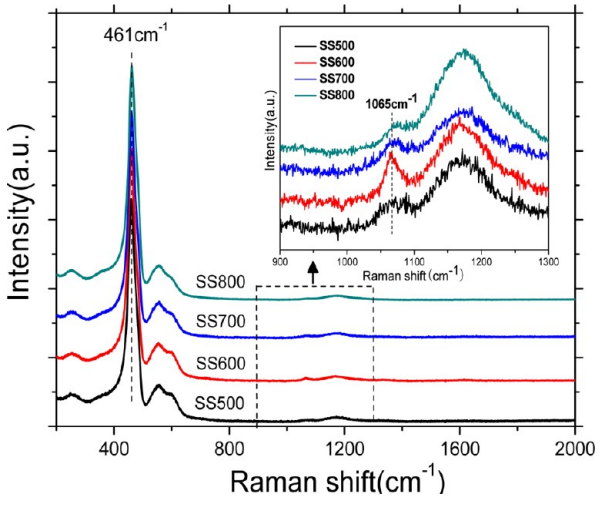

Figure 9. Raman spectra of the sintered SDC/Na_2CO_3 composites after water-soaking.

spectra from 200 to 2000 cm^{-1} and an inset view for details from 800 to 1400 cm^{-1}. It is very intriguing to find that the high Raman peak for SDC crystallites in the samples is now centered at 461 cm^{-1}, almost the same as that for pure SDC powder, and the Raman spectra in the inset view apparently show two diffuse peaks for each, one at 1065 cm^{-1} attributable to Na_2CO_3 and the other at 1170 cm^{-1} to SDC. Evidently, this result, on the one hand, reveals that the microstructure of SDC nanocrystals is quite sensitive to the strong adsorption of carbonate ions and it can be recovered to the states of normal SDC crystallites upon the removal of most carbonates in the SDC/Na_2CO_3 composites. On the other hand, it can be seen that the two characteristic Raman peaks for the amorphous Na_2CO_3 at 1067 and 1077 cm^{-1}, as shown in Figure 8, are now reduced into a single one around 1065 cm^{-1}, which is even weaker in contrast to the Raman band of SDC crystallites at 1170 cm^{-1}. This is because the carbonate molecules situated at larger distance from the surface of SDC crystallites tend to be more dissolved in the soaking treatment because of the relatively weak absorptions. However, it is worthy to note that among the four water-soaked samples, sample SS600 shows the highest intensity for the Raman peak at 1065 cm^{-1}, which was prepared by prefiring at 600 °C and sintering at 680 °C. This result is in a good agreement with the date listed in Table 1, where the sample SS600 has the highest relative integrated intensity, and confirms that it contains the largest amount of carbonate bound to the intimate shell layers characterized by a Raman peak around 1067 cm^{-1}.

As an important supplemental support to the above arguments, the infrared spectra for the SDC/Na_2CO_3 composite samples were recorded and given in Figure 10. It can be seen that the three infrared active vibration modes for the carbonate ions in both the crystalline $NaCO_3$ and the SDC/

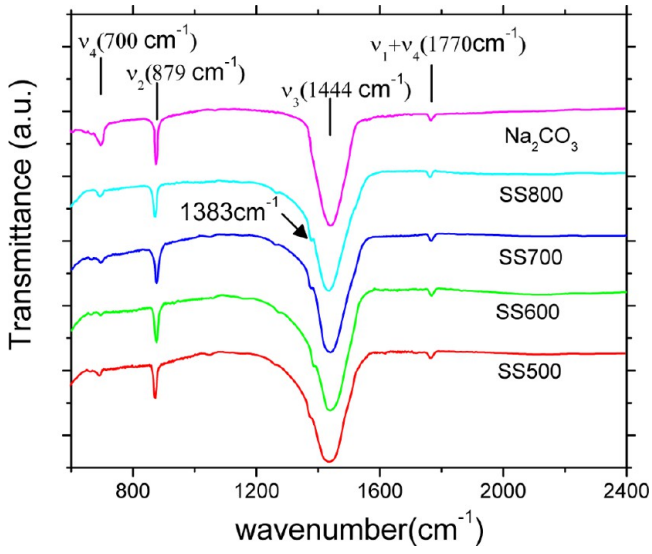

Figure 10. FTIR spectra of the SDC/Na_2CO_3 composites sintered at 680 °C after prefiring at 500, 600, 700, and 800 °C, along with that of crystalline Na_2CO_3 for comparison.

Na_2CO_3 composites samples may be clearly identified, which are ν_2 around 879 cm^{-1} for the polar vibration perpendicular to the plane of the ion, ν_3 around 1440 cm^{-1} and ν_4 around 700 cm^{-1} for the doubly-degenerate modes of asymmetric vibrations in the plane of the ion.[50,51] More interestingly, it is noted that the major absorption bands (ν_3) for the SDC/Na_2CO_3 composites samples all show a remarkably broader peak profile (fwhm ≈ 125 cm^{-1}) and a apparent red-shift of about 4 cm^{-1} compared to that of the crystalline Na_2CO_3 (fwhm ≈ 95 cm^{-1}). In addition, a small shoulder can be noted around 1383 cm^{-1}, as indicated in Figure 10. Evidently, this result provides a supplemental support to the arguments derived from the above Raman spectrum analysis because the similar peak's broadening and red-shifts arising from the distinctive two-mode state dispersion of carbonate ions in the SDC/Na_2CO_3 composites can be observed. However, it is believed that in Figure 10 the two-mode state dispersion of carbonate ions is not shown as clear as that demonstrated in the Raman spectra in Figure 8, since the asymmetrical vibration (ν_3) in the plane of the carbonate ion itself usually shows a very broad absorption band, which makes it difficult to separate well the overlapped peaks.

3.5. Oxide Ion Conductivities of Sintered SDC/Na_2CO_3 Composites. Figure 11 exhibits the typical ac impedance spectra for the sintered SDC/Na_2CO_3 composite samples, which were measured at 500 and 600 °C in air, and therefore, no proton transport may be involved in the conduction of charge carriers. Apparently, these spectra comprise one high frequency incomplete semicircle corresponding to the contribution from the bulk composite and one low frequency arc associated with the electrode process. The high frequency arcs are typical of the coexistence of several processes with different relaxation times, and no impedance component from the usual grain boundaries in a polycrystalline oxide electrolyte can be observed, which should originate from the strong interactions between the phases of SDC crystallites and carbonate. Besides, it can be seen that the ac impedance spectra clearly demonstrate the significant dependence on the prefiring temperature, with the sample SS600 showing the lowest resistances, regardless of the absence of its high-frequency arc at

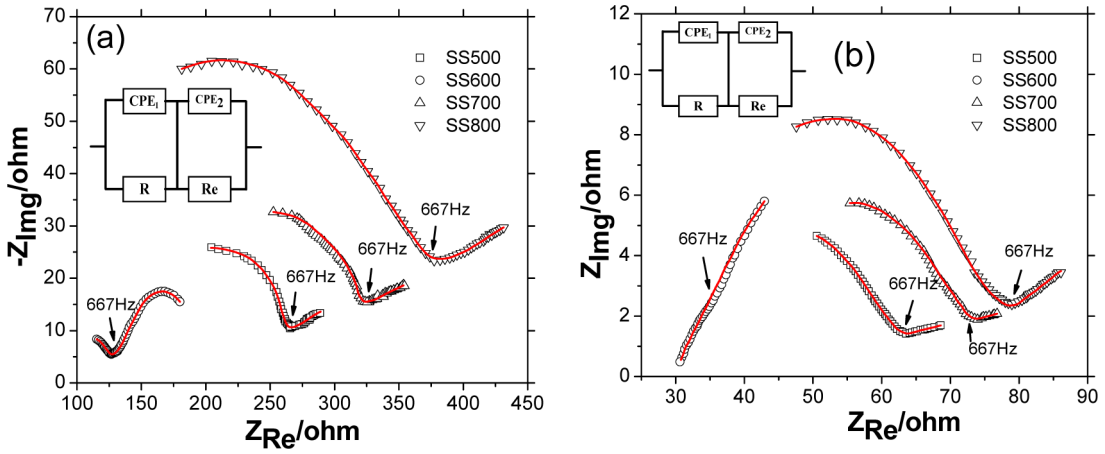

Figure 11. Typical ac impedance spectra of SDC/Na_2CO_3 composites sintered at 680 °C after prefiring at 500, 600, 700, and 800 °C, measured at 500 °C (a) and 600 °C (b), with the equivalent circuits for data-fitting.

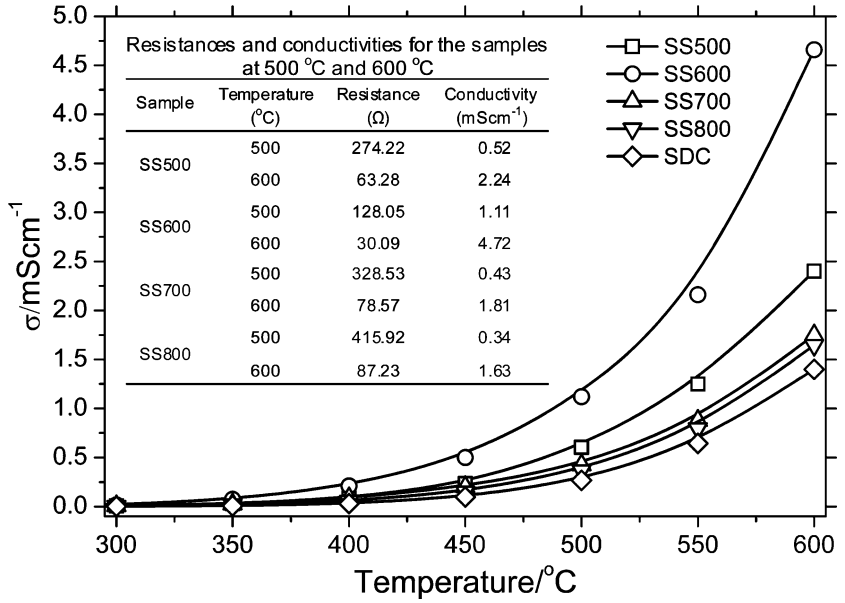

Figure 12. Conductivities of sintered SDC/Na_2CO_3 composites and pure SDC ceramic electrolyte as a function of temperature, together with their values of resistances and conductivities at 500 and 600 °C.

600 °C. On the basis of the above analysis, an equivalent circuit with two $R-Q_{CPE}$ units in series was chosen to fit the impedance data with the resistance R and the pseudo-capacitance Q_{CPE} as the fitting parameters. As the best-fit results, the values of resistance R for the SDC/Na_2CO_3 composite samples were converted into the corresponding conductivities by using the relation $\sigma = L/(RA)$, where L and A are the thickness and end-surface area of the samples, respectively, and presented in Figure 12, together with the conductivity for pure SDC ceramic electrolyte for comparison. Also, some resistance and conductivity data for the samples measured at 500 and 600 °C are given in the table inset in Figure 12.

It can be seen from Figure 12 that the conductivities for the SDC/Na_2CO_3 composite samples are exponentially increased as the temperature increases, manifesting a working mechanism on the thermal activations. Moreover, compared with the oxide ion conductivity of SDC, the conductivities of the composite samples are all significantly enhanced to different extents and the maximum enhancement is realized with the sample SS600, almost 3 times larger than that of the single phase SDC, followed by the samples SS500, SS700, and SS800 in a decreasing sequence of the enhancements. Obviously, this sequence of conductivity enhancements is highly consistent with the relative integrated intensities of Raman peaks around 1067 cm^{-1} for the SDC/Na_2CO_3 composite samples. The higher intensity the Raman peak has, the larger enhancement of conductivity can be realized in the SDC/Na_2CO_3 composite electrolytes. In view of the fact that all the SDC/Na_2CO_3 composite samples have the same phase compositions and are sintered at the same temperature but subjected to the prefiring treatments at different temperatures, it is believed that the prefiring temperature should be an important factor that can significantly affect the ionic conductivities of SDC/Na_2CO_3 composite electrolytes because it could determine the properties of interfacial interactions between the phases of SDC crystallites and carbonate, which are initially created upon the prefiring treatments and closely associated with the particle size of SDC and its specific surface microstructures. As shown in Figure 6, the SS500 and SS600 samples contain the SDC

nanocrystals with an average size of about 30 nm, while the SDC crystallites are about 40 and 60 nm in the SS700 and SS800, respectively. Therefore, one may expect that more conductivity enhancement should be provoked in the SS500 and SS600 than the SS700 and even more than the SS800, since a greater interface area can be built up by the small SDC nanocrystals than the large ones. Evidently, this point is in a good agreement with the above experimental results.

As regards the conductivity difference between the samples SS500 and SS600, in which the SDC crystallites are of nearly the same average size, as shown in Figure 6, it is supposed to be associated with the details of surface microstructures of SDC nanocrystals in the samples. Considering the fact that the SDC nanocrystals are actually bounded by a few different facets and the {100} facets show a stronger attraction to the carbonate ions due to their higher electropositivity than the other facets, it is speculated that the coverage percentage of SDC crystallites by the {100} facets would play a crucial role in the interface interactions and then the enhancement of ionic conductivity of SDC/Na_2CO_3 composites apart from the average size of SDC nanocrystals. Moreover, it could be greatly affected by the conditions of prefiring treatments. The higher prefiring temperature may result in the formation of larger SDC nanocrystals, as shown in Figure 3, but it is confined to a certain limit due to the presence of carbonate phase. Hence, the large SDC crystallites in the sample SS600 just after the prefiring treatment are expected to have more chance to allow the {100} facets to develop during the sintering process than the small ones in the sample SS500. As a consequence, a surface with more {100} facets of high electropositivity is expected to appear for the SDC nanocrystals in the SS600 than in SS500. This point can be supported by Figure 9, where the characteristic Raman peak for sample SS600 shows not only a higher intensity than that of the other samples but a larger red-shift to 1065 cm^{-1} as well. Therefore, it can be concluded that the higher ionic conductivity for the SDC/Na_2CO_3 composite prefired at 600 °C than the other samples may be attributed to the small particle size of SDC crystallites and their more {100} facets on the surface. In this sense, to optimize the prefiring temperature as well as other processing conditions may be an effective way to improve the ionic conductivity of SDC/Na_2CO_3 composites.

In Figure 13 are given the Arrhenius plots $\ln(\sigma T) \sim 1/T$ of electrical conductivities for SDC/Na_2CO_3 composite samples over the temperature range from 200 to 600°C. For the sake of comparison, the data for single phase SDC and the data reported by R. Raza[24] for SDC/Na_2CO_3 composite are also presented. It is very interesting to find that, on the one hand, the pretty straight-line dependences are observed in the whole temperature range for the SDC/Na_2CO_3 composites and the single phase SDC. Moreover, the activation energies from the slopes are found to be approximately the same for the SDC/Na_2CO_3 composite samples, just slightly changing from 0.87 to 0.89 eV, but remarkably lower than that of pure SDC, 1.03 eV, as shown in Figure 13. This result indicates that the SDC/Na_2CO_3 composites possess similar mechanisms for the relevant ionic transportation, regardless of their differences in prefiring temperature. The remarkable decrease in activation energy suggests the presence and positive contribution of the second mechanism for ionic transport at the interface layers between SDC and amorphous carbonate.

On the other hand, however, the Arrhenius plots for the SDC/Na_2CO_3 composite samples in this study are quite

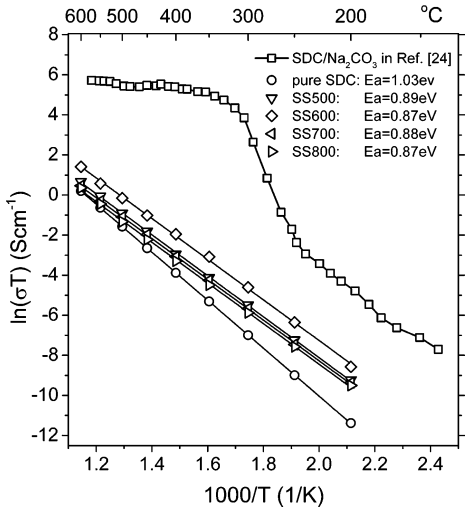

Figure 13. Arrhenius plots for SDC/Na_2CO_3 composites sintered at 680 °C after prefiring at 500, 600, 700, and 800 °C, together with that for pure SDC (in solid circles) and the one reported by ref 24 (in hollow squares) for comparison.

different from the one reported by R. Raza et al.,[24] although its chemical composition and processing conditions were reported as the same as ours. It gives an activation energy close to that for pure SDC below 250 °C, while its conductivity is about 3 orders of magnitude larger than that of pure SDC. This is very strange because it means that the enhanced conductivity in a solid composite of SDC and Na_2CO_3 could be realized even at temperatures lower than 250 °C. In addition, a jump of about 3 orders of magnitude in the $\ln(\sigma T) \sim 1/T$ plot can be noticed in a narrow temperature range around 250°C and it is followed by a conductivity increase with an extremely low activation energy at temperatures over 300 °C. The authors attributed such a conductivity jump to the so-called glass transition of amorphous Na_2CO_3, although this phenomenon is supposed to take place when the carbonate starts to melt into liquid. In the present research, no glass transition has been observed at all either from our DSC curve, as mentioned previously, or from the temperature-dependent conductivity curve, as shown in Figure 13. The similar results were also reported by C. M. Lapa and T. Ristoiu,[52,53] where no change in the Arrhenius plot's slope was found in the concerned temperature range.

4. CONCLUSIONS

In this study, the SDC/Na_2CO_3 nanocomposite electrolytes have been prepared through a rare-earth/sodium carbonate complex precipitation, followed by prefiring and sintering operations. On the basis of structural characterization by XRD, FESEM, TEM, and TG-DSC, the interfacial interactions between the phases of SDC nanocrystals and amorphous carbonate were probed by Raman and infrared spectroscopies. According to the experimental results and related discussions, the following main conclusions may be drawn:

(1) In the as-prepared SDC/Na_2CO_3 nanocomposite electrolytes, SDC nanocrystals with the average sizes across 30−60 nm are highly compacted into three-dimensional homogeneous structures with the voids and gaps fully infiltrated by the amorphous carbonate phase. The carbonate is tightly bound to the surface of SDC nanocrystals because of the strong long-range interface interactions to form a core−shell structure with an intimate layer of ∼8 nm in thickness, but no glass

transition can be found by DSC and temperature-dependent conductivity analyses.

(2) The SDC/carbonate interface interactions render the Raman vibration mode of the carbonate ions to shift and form two peaks at 1067 and 1077 cm^{-1} with respect to 1081 cm^{-1} for the crystalline Na_2CO_3. Such red-shifts are attributed to the binding effects on the adsorbed carbonate and may serve as a measure of the strength for the interface interactions, which is supposed to give rise to the noncrystallization of carbonate in the SDC/Na_2CO_3 composite electrolytes and their conductivity enhancements.

(3) The intimate layers of carbonate bound on the surface of SDC nanocrystals are believed to determine the crucial contributions to the conductivity enhancements for SDC/Na_2CO_3 composites, and they can be quantified by the relative integrated intensity of the Raman peak around 1067 cm^{-1}. The higher the peak intensity is, the higher conductivity enhancement can be accomplished in the SDC/Na_2CO_3 composite electrolytes.

(4) Smaller SDC nanocrystals are found to achieve higher conductivity enhancements for the SDC/Na_2CO_3 composite electrolytes. But the {100} facets on the surface of SDC nanocrystals are believed to be more important than other facets because of their strong electropositivity, which can greatly affect the interfacial interactions and then enhance the ionic conduction in the composite electrolytes.

(5) The prefiring temperature can effectively influence the growth of SDC nanocrystals in the SDC/Na_2CO_3 composites and the formation of their {100} facets. It allows the SDC/Na_2CO_3 composites prefired at 600 °C to reach a much higher ionic conductivity than the other samples, about 3 times higher than that of the pure SDC, because of more development of the {100} facets. Optimization of the prefiring temperature as well as other processing conditions may be an effective way to further improve the ionic conductivity of SDC/Na_2CO_3 composites.

AUTHOR INFORMATION

Corresponding Author

*E-mail: zengyanwei@tom.com. Phone: +86 25 83587254. Fax: +86 25 83587254.

Notes

The authors declare no competing financial interest.

ACKNOWLEDGMENTS

The authors gratefully acknowledge the funds by the Priority Academic Development Program of Jiangsu Higher Education Institutions, P. R. China, the Program for Changjiang Scholars and Innovative Research Teams in Universities (PCSIRT) of China, Grant IRT1146, and the Program of Research Innovation for University Graduate Students of Jiangsu Province (No. CXZZ11_0331).

REFERENCES

(1) Chroneos, A.; Yildiz, B.; Tarancón, A.; Parfitt, D.; Kilner, J. A. *Energy Environ. Sci.* **2011**, *4*, 2774−2789.

(2) Wachsman, E. D.; Lee, K. T. *Science* **2011**, *334*, 935−939.

(3) Aravind, P. V.; de Jong, W. *Prog. Energy Combust. Sci.* **2012**, *38*, 737−764.

(4) Wei, H. Z.; Zeng, Y. W.; Wang, L.; Cai, T. X.; Sun, X. L. *Adv. Colloid Interface Sci.* **2010**, *161*, 181−194.

(5) Yang, W.; Hong, T.; Li, S.; Ma, Z. H.; Sun, C. W.; Xia, C. R.; Chen, L. Q. *ACS Appl. Mater. Interfaces* **2013**, *5*, 1143−1148.

(6) Shao, Z. P.; Zhou, W.; Zhu, Z. H. *Prog. Mater. Sci.* **2012**, *57*, 804−874.

(7) Fergus, J. W. *J. Power Sources* **2006**, *162*, 30−40.

(8) Fukuda, K.; Asaka, T.; Hamaguchi, R.; Suzuki, T.; Oka, H.; Berghout, A.; Béchade, E.; Masson, O.; Julien, I.; Champion, E.; Thomas, P. *Chem. Mater.* **2011**, *23*, 5474−5483.

(9) Meng, G. Y.; Fu, Q. X.; Zha, S. W.; Xia, C. R.; Liu, X. Q.; Peng, D. K. *Solid State Ionics* **2002**, *148*, 533−537.

(10) Zhu, B.; Yang, X. T.; Xu, J.; Zhu, Z. G.; Ji, S. J.; Sun, M. T.; Sun, J. C. *J. Power Sources* **2003**, *118*, 47−53.

(11) Huang, J. B.; Yang, L. Z.; Gao, R. F.; Mao, Z. Q.; Wang, C. *Electrochem. Commun.* **2006**, *8*, 785−789.

(12) Benamira, M.; Ringuedé, A.; Albin, V.; Vannier, R. N.; Hildebrandt, L.; Lagergren, C.; Cassir, M. *J. Power Sources* **2011**, *196*, 5546−5554.

(13) Fan, L. D.; Zhang, G. Q.; Chen, M. M.; Wang, C. Y.; Di, J.; Zhu, B. *Int. J. Electrochem. Sci.* **2012**, *7*, 8420−8435.

(14) Ferreira, A. S. V.; Soares, C. M. C.; Figueiredo, F. M. H. L. R.; Marques, F. M. B. *Int. J. Hydrogen Energy* **2011**, *36*, 3704−3711.

(15) Zhang, L.; Lan, R.; Xu, X.; Tao, S.; Jiang, Y.; Kraft, A. *J. Power Sources* **2009**, *194*, 967−971.

(16) Liu, W.; Liu, Y.; Li, B.; Sparks, T. D.; Wei, X.; Pan, W. *Compos. Sci. Technol.* **2010**, *70*, 181−185.

(17) Raza, R.; Wang, X.; Ma, Y.; Zhu, B. *J. Power Sources* **2010**, *195*, 6491−6495.

(18) Yin, S. L.; Ye, Z. P.; Li, C. M.; Chen, X. W.; Zeng, Y. W. *Mater. Lett.* **2013**, *92*, 78−81.

(19) Cai, T. X.; Zeng, Y. W.; Yin, S. L.; Wang, L.; Li, C. M. *Mater. Lett.* **2011**, *65*, 2751−2754.

(20) Huang, J. B.; Mao, Z. Q.; Liu, Z. X.; Wang, C. *Electrochem. Commun.* **2007**, *9*, 2601−2605.

(21) Di, J.; Chen, M.; Wang, C.; Zheng, J.; Fan, L.; Zhu, B. *J. Power Sources* **2010**, *195*, 4695−4699.

(22) Xia, C.; Li, Y.; Tian, Y.; Liu, Q. H.; Wang, Z. M.; Jia, L. J.; Zhao, Y. C.; Li, Y. D. *J. Power Sources* **2010**, *195*, 3149−3154.

(23) Raza, R.; Wang, X.; Ma, Y.; Liu, X.; Zhu, B. *Int. J. Hydrogen Energy* **2010**, *35*, 2684−2688.

(24) Wang, X. D.; Ma, Y.; Raza, R.; Muhammed, M.; Zhu, B. *Electrochem. Commun.* **2008**, *10*, 1617−1620.

(25) Zuo, N.; Zhang, M. L.; Mao, Z. Q.; Gao, Z.; Xie, F. C. *J. Eur. Ceram. Soc.* **2011**, *31*, 3103−3107.

(26) Ma, Y.; Wang, X.; Raza, R.; Muhammed, M.; Zhu, B. *Int. J. Hydrogen Energy* **2010**, *35*, 2580−2585.

(27) Huang, J.; Gao, Z.; Mao, Z. *Int. J. Hydrogen Energy* **2010**, *35*, 4270−4275.

(28) Zhu, B. *Int. J. Energy Res.* **2006**, *30*, 895−903.

(29) Wang, X.; Ma, Y.; Li, S.; Kashyout, A.; Zhu, B.; Muhammed, M. *J. Power Sources* **2011**, *196*, 2754−2758.

(30) Liu, Q.; Zhu, B. *Appl. Phys. Lett.* **2010**, *97*, 183115.

(31) Benamira, M.; Ringuedé, A.; Hildebrandt, L.; Lagergren, C.; Vannier, R.-N.; Cassir, M. *Int. J. Hydrogen Energy* **2012**, *37*, 19371−19379.

(32) Huang, J. B.; Xie, F. C.; Wang, C.; Mao, Z. Q. *Int. J. Hydrogen Energy* **2012**, *37*, 877−883.

(33) Zhao, Y. C.; Xia, C.; Wang, Y. J.; Xu, Z. R.; Li, Y. D. *Int. J. Hydrogen Energy* **2012**, *37*, 8556−8561.

(34) Zhao, Y. C.; Xia, C.; Xu, Z. R.; Li, Y. D. *Int. J. Hydrogen Energy* **2012**, *37*, 11378−11382.

(35) Jing, Y. F.; Patakangas, J.; Lund, P. D.; Zhu, B. *Int. J. Hydrogen Energy* **2013**, *38*, 16532−16538.

(36) Khan, M. A.; Raza, R.; Lima, R. B.; Chaudhry, M. A.; Ahmed, E.; Abbas, G. *Int. J. Hydrogen Energy* **2013**, *38*, 16524−16531.

(37) Ferri, D.; Grenthe, I.; Hietanen, S.; Salvatore, F. *Acta Chem. Scand., Ser. A* **1983**, *37*, 359−365.

(38) Kumar, A.; Babu, S.; Karakoti, A. S.; Schulte, A.; Seal, S. *Langmuir* **2009**, *25*, 10998−11007.

(39) Mineshige, A.; Taji, T.; Muroi, Y.; Kobune, M.; Fujii, S.; Nishi, N.; Inaba, M.; Ogumi, Z. *Solid State Ionics* **2000**, *135*, 481−485.

(40) Dubbledam, G. C.; De Wolff, P. M. *Acta Crystallogr. B* **1969**, *25*, 2665−2667.
(41) Buzgar, N.; Apopei, A. I. *An. Stiint. Univ. "Al. I. Cuza" Iasi* **2009**, *55*, 97−112.
(42) Meekes, H.; Rasing, T.; Wyder, P.; Janner, A.; Janssen, T. *Phys. Rev. B* **1986**, *34*, 4240−4254.
(43) Sayle, D. C.; Maicaneanu, S. A.; Watson, G. W. *J. Am. Chem. Soc.* **2002**, *124*, 11429−11439.
(44) Lee, W. H.; Shen, P. *J. Cryst. Growth* **1999**, *205*, 169−176.
(45) Baudin, M.; Wójcik, M.; Hermansson, K. *Surf. Sci.* **2000**, *468*, 51−61.
(46) Ahniyaz, A.; Sakamoto, Y.; Bergstrom, L. *Cryst. Growth Des.* **2008**, *8*, 1798−1800.
(47) de Carolis, S.; Pascual, J. L.; Pettersson, L. G. M.; Baudin, M.; Wójcik, M.; Hermansson, K.; Palmqvist, A. E. C.; Muhammed, M. *J. Phys. Chem. B* **1999**, *103*, 7627−7636.
(48) Cheng, J. R.; He, L.; Yu, S. W.; Meng, Z. Y. *Appl. Phys. Lett.* **2006**, *88*, 152906.
(49) Cotton, F. A. *Chemical Applications of Group Theory*, 3rd ed.; Wiley-Interscience: New York, 1990.
(50) Harris, M. J.; Salje, E. K. H. *J. Phys.: Condens. Matter* **1992**, *4*, 4399−4408.
(51) Al-Hawery, A. S. *Jpn. J. Appl. Phys.* **1998**, *37*, 858−862.
(52) Lapa, C. M.; Figueiredo, F. M. L.; de Souza, D. P. F.; Song, L.; Zhu, B.; Marques, F. M. B. *Int. J. Hydrogen Energy* **2010**, *35*, 2953−2957.
(53) Ristoiu, T.; Petrisor, T., Jr.; Gabor, M.; Rada, S.; Popa, F.; Ciontea, L.; Petrisor, T. *J. Alloys Compd.* **2012**, *532*, 109−113.